



**Materials
Horizons**

Passivation-Driven Speciation, Dealloying and Purification

Journal:	<i>Materials Horizons</i>
Manuscript ID	MH-COM-11-2020-001832.R1
Article Type:	Communication
Date Submitted by the Author:	08-Jan-2021
Complete List of Authors:	Martin, Andrew; Iowa State University Chang, Boyce; Iowa State University, Materials Science and Engineering Cutinho, Joel; Iowa State University, Materials Science and Engineering SHEN, LIYANG; Iowa State University, Chemical and Biological Engineering Ward, Thomas; Iowa State Univ, Aerospace Engineering Cochran, Eric; Iowa State University, Chemical and Biological Engineering; Thuo, Martin; Iowa State University, Materials Science and Engineering

SCHOLARONE™
Manuscripts

New Concept

This work demonstrates the role of surfaces as a dissipation horizon. Through the presence of energy and composition gradient within the passivating surface layers in metals, mass transport and redox-driven enrichment is attained in metallic alloy systems. Utilizing natural phenomenon of oxidation and diffusion in metal, facile speciation, dealloying and purification method can be achieved. This process creates unique pathway in synthesizing pure metallic system out of an alloy using thermal expansion mismatches or unique metal oxide species using a 'ship-in-a-bottle' method. This concept can be utilized as an alloy design parameter to create stimuli-responsive materials with selective reactivity upon trigger.

COMMUNICATION

Passivation-Driven Speciation, Dealloying and Purification

Andrew Martin,^a Boyce Chang,^a Joel Cutinho,^a Liyang Shen,^b Thomas Ward III,^c Eric W. Cochran,^b Martin M. Thuo^{*a,d,e}Received 00th January 20xx,
Accepted 00th January 20xx

DOI: 10.1039/x0xx00000x

Thin passivating surface oxide layers on metal alloys form a dissipation horizon between dissimilar phases, hence harbour an inherent free energy and composition gradient. We exploit this gradient to drive order and selective surface separation (speciation), enabling redox-driven enrichment of the core by selective conversion of low standard reduction potential (E°) components into oxides. Coupling this oxide growth to volumetric changes during solidification allows us to create oxide crystallites trapped in a metal ('ship-in-a-bottle') or extrusion of metal fingerlings on the heavily oxidized particle. We confirm the underlying mechanism through high temperature X-ray diffraction and characterization of solidification-trapped particle states. We demonstrate that engineering the passivating surface oxide can lead to purification via selective dealloying with concomitant enrichment of the core, leading to disparate particle morphologies.

Introduction

Passivating metal oxides are paradoxical entities in that they offer protection from corrosion – on condition that they do not spall or crack, but they deplete a metal (albeit minimally in most cases) and introduce interfaces with significantly different properties than the bulk.^{1, 2} These oxides are a thermodynamically different entity from the bulk, yet at ambient are fixed component of the metal.^{3, 4} Despite their small (nm) sizes, they have been utilized to stabilize metastable states⁵ or alter properties of liquid metals,^{1,6-9} leading to new unprecedented applications.¹⁰⁻¹⁵ Structural complexity in these nanoscale passivating oxide layers has, however, only been

recently described albeit in liquid metals.^{2, 7, 16, 17} Through felicitous choice of processing conditions, autonomous Thermal Oxidative Composition Inversion (TOCI) and surface texturing^{18, 19} empirically confirmed this complexity and highlights underlying speciation (that is distribution and/or organization of alloy elements or mixed oxidation states)²⁰ by externally exuding these gradients. By exploiting relation between mass and energy ($E \propto m$), the composition gradient must lead to asymmetry in mass distribution hence a sharp energy gradient across the thin passivating layers. The energy gradient in turn can frustrate relaxation and equilibration leading to metastable material states.^{1, 5, 12, 21} This ansatz has been demonstrated through stabilization of undercooled metal particles,¹⁵ that have enabled low-temperature metal processing.^{12, 15, 21} The inferences above, however, are premised on the outward growth of a thin (<20 nm) passivating oxide layer that is, Cabrera-Mott type oxidation,²² but speciation under thicker (>1 μm) oxide layers has not been demonstrated.

Surface oxidation of metals is mechanistically understood as a thickness-dependent asymmetric flux process in that, initially metal ions and/or electrons flux/migrate to the oxide-ambient surface and/or oxidant diffuses towards the oxide-metal interface.²²⁻²⁵ The former is well captured by the Cabrera-Mott oxidation theory²⁶ (Figure 1a) and, as expected, is limited to thin (<20 nm) oxide films. The latter dominates with thicker (>1 μm) oxides as described by the Wagner's oxidation theory (Figure 1c).²⁷⁻³² The intermediate region (20 nm < thickness < 1 μm) has been captured as a rate-law differentiated transition regime (Xu-Rosso-Bruemmer postulate²² – abbreviated XRB postulate, Figure 1b). The Cabrera-Mott and Wagner oxidation regimes follow an inverse logarithmic and a parabolic growth rate law respectively. The transition regime, however, follows a direct logarithmic growth rate.²² Factors that determine direction of ionic diffusion during the oxidation event have been shown to heavily depend on the potential and mobility differences between the metal cations (M^+) and oxygen anions (O^{2-}).^{22, 26, 28-30} Nature of atomic interactions, alloy composition, passivating oxide thickness and associated speciation, may also affect ionic diffusion. All these mechanisms, however, presume the existence of a native metal oxide film (Figure 1a-c). On a bare alloy surface, stoichiometry and stochasticity (equalling *a priori*

^a Department of Materials Science and Engineering, Iowa State University, Ames, IA-50010. USA

^b Department of Chemical and Biological Engineering, Iowa State University, Ames, IA-50010. USA

^c Department of Aerospace Engineering, Iowa State University, Ames, IA-50010. USA

^d Micro-Electronics Research Center, Ames, IA-50010. USA

^e Department of Electrical and Computer Engineering, Iowa State University, Ames, IA-50010. USA

Electronic Supplementary Information (ESI) available: Materials and methods, raw SEM images and more detailed experiments are available in the SI. See DOI: 10.1039/x0xx00000x

probabilities for all alloy components to react) drive surface oxidation. This initial oxidation captures both composition and redox potential differences, setting up a surface speciation due

to asymmetry in reactivity and diffusion (upon depletion of the topmost layer) that has not been captured until recently.^{2, 16}

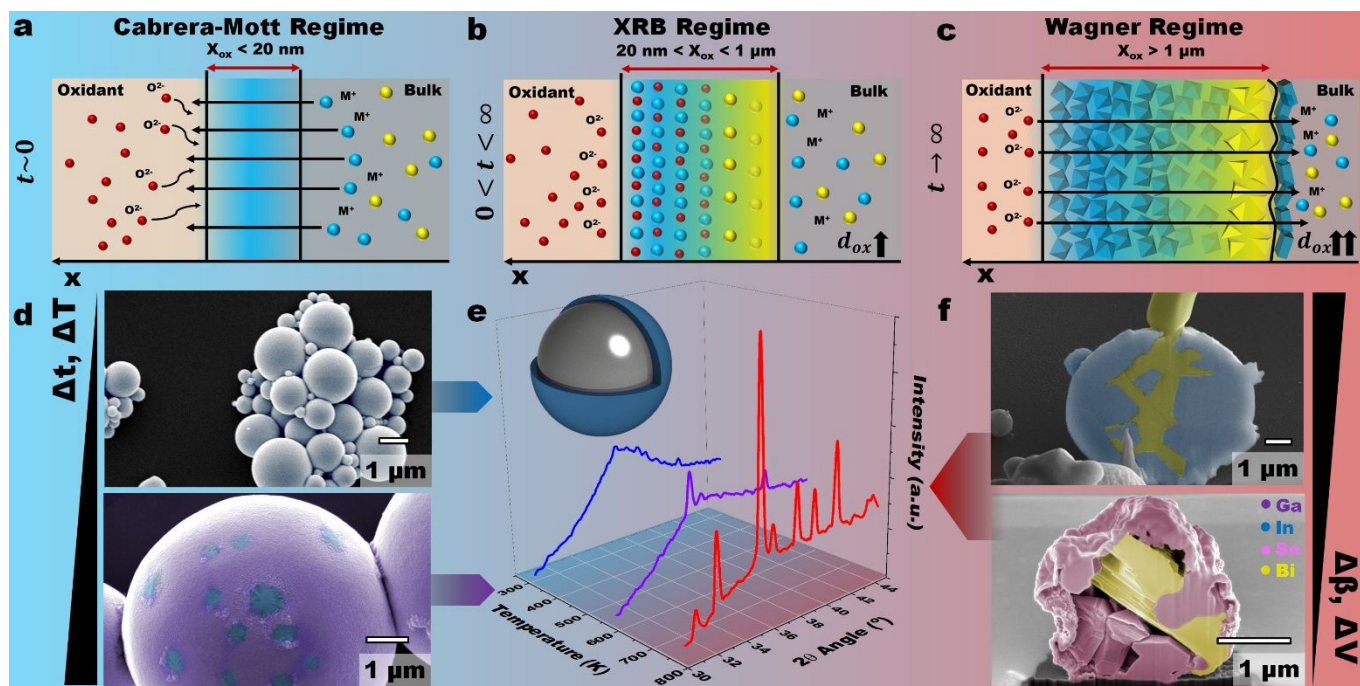


Figure 1. Schematic of different oxidation processes at different times (t); (a) Cabrera-Mott regime during early oxidation stage, (b) XRB regime during intermediate stage and (c) Wagner regime at late oxidation stage. (d) SEM images of control particles (top) and oxidized particles (bottom) showing emergence of a new layer. (e) HTXRD of particles indicating different oxidation stages. (f) Product of extended oxidation with different alloys such as Field's metal (top) and BiSn (bottom). False coloring: blue indicates native, indium rich oxide, purple: first tier growth rough gallium oxide, yellow: bismuth rich region and pink: tin rich region. (d_{ox} = oxide thickness, t = time, T = temperature, β = volumetric thermal expansion coefficient, V = volume).

We inferred that the proposed asymmetric ionic and oxidant diffusion (Figure 1a-c) should manifest as perturbations to the metal-oxide interfaces. In an alloy system, however, differences in standard reduction potential (E^0) should induce a kinetically resolved differentiation and speciation. This differentiation in turn leads to concentration gradients across the oxide, with the surface being dominated by the most reactive component with concomitant enrichment of higher E^0 component(s) at the metal-oxide interface.^{2, 16, 33} This ansatz, however, hinges on unrestricted diffusion of the alloy components—hence, the need for high plasticity at the metal-oxide interface.³⁴ Liquid metals offer such an interface and are therefore ideal testbeds for this hypothesis.^{7, 17, 35, 36} A caveat with liquid metals, however, is that surface plasticity and the fluidic state renders post speciation characterization challenging.³⁴ Coupling this process to a phase change, however, arrests the metallic components in a form that cannot reconstitute post synthesis. Introducing a solidification step also allows one to capture physical changes due to negative (e.g. in Bi rich phases) or positive (e.g. Sn) thermal expansion.³⁷ In the former, surface features akin to those observed during TOCI, but in non-oxidized form, are expected irrespective of the oxide thickness. In the latter, under the Wagner oxidation regime and extended oxide growth, entrapment of oxide crystallites inside metals is expected – akin to ‘ship-in-a-bottle’, as the metal solidifies around stalagmite/stalactite-like oxide protuberances.

Depending on the orientation of the oxide crystallites relative to the molten component, the metal can solidify around the crystals leading to a tightly bound oxide-in-metal structure. With selective enrichment of the low E^0 element into the oxide, hence dealloying, we infer that growing oxide crystallites can be engulfed by a metallic component rich in higher E^0 component(s)—a fete that is otherwise impossible especially at the nano- to meso-scale. This speciation, however, hinges on the inward growth of the crystallites (Wagner regime) hence the oxide layer needs to be significantly thick. We infer that this will likely occur for alloys with significantly larger amounts of the lower E^0 component. Beside growth kinetics, thermo-expansive work (thermal fatigue) initiated defects also affects resultant mass distribution, and uniform oxide growth.

Recent advances in the understanding of surface speciation during the oxidation process further suggest that the evolution of the surface oxide may lead to bulk or subsurface enrichment in the higher E^0 component of the alloy.^{2, 16, 18, 19} This autonomous speciation also manifests in the evolution in composition of surface oxides on liquid metal particles (Figure 1d).^{18, 19} We infer that this auto-speciation can lead to surface-driven de-alloying, hence changes in the bulk composition. In the case of negative thermal expansion core, the enriched component will stress and may break through the oxide shell on solidification, presenting metallic features on the surface—that is, an inversion in component distribution (Figure 1f, top).

Where phase change leads to contraction of the core, the oxide implodes (ductile shell) or cracks (brittle shell) trapping a metallic component (Figure 1f, bottom). Herein, we demonstrate these phase-change arrested configurations through felicitous choice of alloys and processing conditions.

Negative Thermal Expansion (NTE)

Field's metal (Bi: 32.5, In: 51, Sn: 16.5 wt%, or Bi: 21, In: 60.1, Sn: 18.8 at%, $T_m = 335$ K) shows positive volumetric thermal expansion ($+\beta$, PTE), while Bi (highest E^0 element) shows a negative thermal expansion ($-\beta$, NTE).³⁸ We inferred that controlled dealloying by growth of the passivating oxidation deep into the Wagner regime, at $T > T_m$, would lead to In ($E_{In}^0 = -0.34$, $|\beta_{In}| = 33 \cdot 10^{-6} \text{ K}^{-1}$) and Sn ($E_{Sn}^0 = -0.14$, $|\beta_{Sn}| = 22 \cdot 10^{-6} \text{ K}^{-1}$) oxides with concomitant enrichment of Bi ($E_{Bi}^0 = 0.32$, $|\beta_{Bi}| = 13.2 \cdot 10^{-6} \text{ K}^{-1}$) in the liquid core due to its comparatively higher positive E^0 (Table S1). Compared to the commonly used gallium based liquid metals where the surface is highly dominated by the gallium oxide species ($\sim 0.7 - 2 \text{ nm}$),^{2, 16} undercooled Field's metal's oxide layer tends to be slightly thicker ($\sim 4 - 5 \text{ nm}$),¹ hence transition out of the Cabrera-Mott regime is likely to occur faster. Upon solidification, Bi expands while the oxides contract leading to exudates of solidifying Bi-rich phase (Figure 1f, top).^{18, 19, 38} To illustrate this dealloying/purification, speciation, and solidification-driven inversion of component distribution, undercooled Field's metal particles were synthesized using the SLICE (Shearing Liquid Into Complex particlEs) method.³⁹ The particles were $\sim 1.01 \pm 1.35 \mu\text{m}$ in diameter with solidification temperature of 224 K (Figure S1). These particles bear a thin ($< 5 \text{ nm}$) deformable oxide shell akin to oxidation in the Cabrera-Mott regime.¹ For clarity, all particle images are false colored (see SI for non-colored version) to highlight evolution in surface features. These particles were heated under low oxygen ($\leq 10 \text{ ppm}$) over 573–1273 K range and samples were characterized at 100 K increments (Figure S2).^{18, 19} For comparison, the particles were heated continuously at (10 K/min) to the target temperature with equilibration time, t_e , = 0, 15, 30 or 45 mins (Figure 2 and S2). For brevity and clarity, the 0- and 30-mins samples are compared (Figure 2) while others are given in the supporting information. Deformation and cracks are observed when particles are heated to 573 K and $t_e = 0$ mins (Figure 2a). The extent and distribution of these fractures is exacerbated for $t_e = 30$ mins (Figure 2a_{ii}). These features are in part due to effect of thermal expansivity of a fragile oxide shell. We infer that thicker oxide shells would retain their shape and dissipate stress through cracks, fractures or spalling, increasing oxidant permeability or if core is liquidus and under tension, extrude underlying/bulk components as observed in TOCI.^{18, 19} When particles were heated to 773 K and $t_e = 0$ mins, Bi rich surface features appear (Figure 2b_i), suggesting that the core is rich in Bi. Formation of Bi-rich features is enhanced at $t_e = 30$ mins (Figure 2b_{ii}). Similarly, at $T = 873 \text{ K}$ and $t_e = 0$ mins an increase in the number of Bi-rich surface features increases, while at $T = 873 \text{ K}$ and $t_e = 30$ mins leads to increase in the size (length and/or width) of these surface features (Figure 2c and S2).

At 873 K and $t_e = 30$ mins, we observe that particles that evolve fewer surface features grow a dendrite-like structure (Figure 2c_{ii}), confirming that these features emanate from stress dissipation from the bulk. Given that these features are rich in Bi, an NTE element, vindicates mismatch in thermal expansivity—and associated stresses in this evolution (Table S1). To confirm that these features are related to solidification and originate in the core, first, we sequentially sectioned a particle from the edge through the core (Figures 2e, S3 and Supporting Video SV1). We observed that, as hypothesized, these features originate from or are connected to the core and are released to the surface via fissure-like paths (Figure 2e). We infer that Bi is likely nucleating at the core and, during solidification, induces a solidification-driven mechanical tension due to phase change, σ_{PT} , leading to extrusion of the core with cooling and further solidification. Contraction of the oxide shell with cooling exacerbates σ_{PT} leading to fracture-driven stress dissipation. We infer that more Bi-rich exudates, albeit smaller in size, occur when multiple release points are formed on the oxide, otherwise the Bi features are larger when the release points are limited (conservation of matter). To confirm this inference, we sectioned two particles processed under the same conditions ($T = 873 \text{ K}$ and $t_e = 30$ mins) but differing in the size, shape and number of surface features (Figure S3 and supporting video SV1). We observe that irrespective of the morphology of the features, they originate from the core and are released via fissures forming across the oxide shell. In the absence of the surface features ($T = 573 \text{ K}$), however, a cross-section of the particle shows no centrally placed composition dissimilar feature (Figure S4). Similarly, when compared to a solid particle derived from the SLICE method, only expected spinodal patterns are observed (Figure S5) as previously observed.³⁹ These control experiments support the inference that the observed features, speciation and surface texture changes are not due to the particle preparation method but are due to increased oxidation and solidification of a liquid core.

Compositional mapping using Energy Dispersive x-ray Spectroscopy (EDS) reveals that the exudates are rich in Bi while the rest of the particle is rich in In-Sn. Low oxygen concentration in the exudates suggesting that they are likely metallic Bi that oxidizes upon extrusion (Figure 3a and S6). To closely understand these temperature dependent changes, we characterized the process using: i) coupled Differential Scanning Calorimetry-Thermogravimetric Analysis and InfraRed - Mass Spectrometry (DSC-TGA-IR-MS) and ii) High Temperature X-Ray Diffraction (HTXRD). The DSC-TGA-IR-MS captures mass and energy change with temperature while concomitantly characterizing volatile gases exudates by IR and MS, allowing us to compare the underlying process to the recently reported TOCI. Evolution in the identity and/or crystallinity of the surface oxide is captured via HTXRD. Minor ($\sim 1.4 \%$) and major ($\sim 14.5 \%$) exothermic mass gain events are observed at *ca.* 473 K and 773 K respectively (Figure 3b). These events are analogous to previous patterns observed with other liquid metals.¹⁹ The minor peak at ($\sim 450\text{--}550 \text{ K}$) leads to a spike in gaseous exudates as captured by the Gram-Schmidt plot (Figure 3b). Since the minor peak corresponds to an MS spectrum dominated by m/z

= 44 amu (Figure S7a), we infer a likely loss of surface ligand with concomitant increase in oxide growth as previously observed.¹⁹ The major peak (~600–800 K) is likely a continuous oxide growth as no volatile exudates are captured in the Gram Schmidt plot, MS, and IR spectra (Figure S7a-b). The mass increase plateaus at ~800 K suggesting a change in the oxidation rate. Interestingly, these temperatures coincide with formation of cracks and Bi-rich surface features on the particles that are cooled back to ambient.

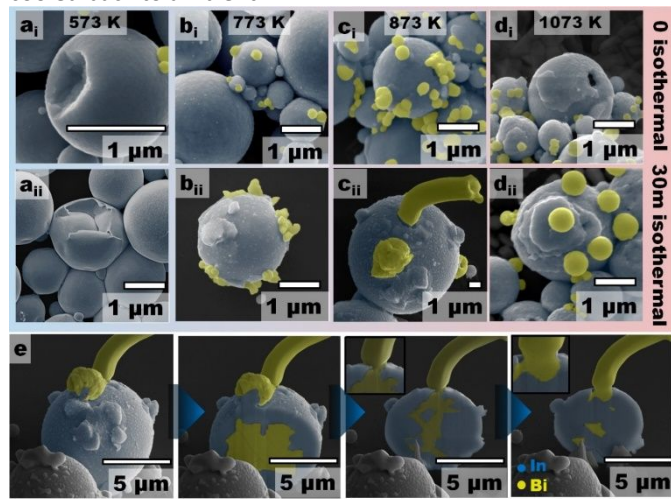


Figure 2. SEM Micrographs of heat-treated Field's metal particles ranging from (a) 573 K, (b) 773 K, (c) 873 K and (d) 1073 K. (i-ii) Indicates 0- and 30-minutes isothermal time respectively. (e) FIB section cut of particle shown in (c_{ii}). False colored images are done to enhance composition difference. False coloring: blue indicates native, indium rich oxide and yellow: bismuth rich region.

To confirm that the oxide shell is growing and playing a critical role, we estimate changes in thickness using Small-Angle X-ray Scattering (SAXS) dimensional analysis through Ruland's method (details in the supporting information).^{40,41} Existence of a diffuse boundary correlates with a negative deviation from ideal Porod's law constant ($\alpha = 4$), where α is the negative power of the scattering vector q , to which the scattered intensity $I(q)$ is proportional ($q^{-\alpha} \propto I(q)$). These values are obtained through curve fitting and correspond to the slope of $\ln I$ vs. $\ln q$ (Figure 3c).⁴² It can be seen that $|\alpha|$ increases as the particles are heated to 523 K (from 4.33 to 4.64), indicating a growing oxide shell. The deviation, however, decreases as the particles reaches 773 K and even further to 1023 K, almost reaching the ideal value. We infer that at 773 K, the oxide has reached a critical thickness upon which it is no longer diffuse or a second process (e.g. sintering or crystallization) counters any increase in thickness due to continued oxidation. Alternatively, the oxides likely form large crystalline structures (Wagner's regime) hence lack a diffuse boundary with the bulk metal hence no deviation in the scattering plot. Approximation of the boundary thickness was done using Ruland's method (Figure S7c) where it displays ~7 nm thick passivating oxide shell at ambient that grows to ~10 nm at 523 K. At 773 K and beyond, the plot displays a straight horizontal line, which gives no approximation of oxide thickness (oxide is too thick). We can therefore infer that at 773 K the oxidation is no longer in the Cabrera-Mott regime, but most likely transitioned to the Wagner regime, which is also indicated by the rapid mass

growth between 600 and 800 K (Figure 3b). Based on the mechanism of the Wagner regime, non-uniform growth of the oxide is likely as surface defects increases access of oxidant diffusion into the oxide-metal interface leading to loss of the diffuse interfacial boundary and localized accelerated growth of oxide crystallites. This inference would lead to stalagmite-stalactite like structures growing into the molten metal core with concomitant continued E^0 -dependent dealloying as components oxidize and nucleate onto these crystallites. The interior of the particle, therefore, adopts a liquid-filled speleothem-like (cave-like) formation at high temperatures. Upon cooling, and solidification, the final structure depends on whether the core is an NTE or PTE component.

To further support this claim, we monitored oxide growth via *in-situ* HTXRD. Samples were heated at 10 K/min and analyzed at increments of 50 K—with the sample allowed to equilibrate for ~20 minutes at each stage while the diffraction pattern is obtained. Using the as-prepared particles as a control, we monitored crystallization of the oxide shell. Fitting the emerging peaks to known oxides informed our inferences as to which component is crystallizing at what temperature (Figure 3d). Obtained data complements TGA-IR-MS in that two transition points are observed during heating. The amorphous material shows no significant change in the diffraction patterns up to ~523 K. For Field's metal, peaks aligning with In_2O_3 are the first to emerge, further supporting previous spectroscopic (Auger and x-ray photo-electron)- and indirect empirical (TOCI)-based inferences on redox-driven surface speciation.¹⁸ These peaks continue to grow in intensity up to 773 K where SnO_2 peaks emerge. Similarly, these data agree with previous SEM, TGA-IR-MS-DSC and SAXS analysis. Alongside the SnO_2 formation at 773 K, a small peak associated with Bi_2O_3 is observed. Surprisingly, this peak further increases upon cooling the sample indicating continued growth of the bismuth oxide. This increased growth occurs alongside appearance of Bi (012, 111 and 104) peaks further suggesting that as Bi solidifies, it is being extruded which upon oxidation leads to enhanced Bi_2O_3 peaks. This data leads us to infer that the exudates are a consequence of solidification of an NTE component in a tightly closed shell. When the sample is cooled to room temperature all peaks experience a small shift due to thermal contraction. From the data above we confirm; i) selectivity in the formation of the oxide components correlates to redox potential ($E_{\text{In}}^0 = -0.34 < E_{\text{Sn}}^0 = -0.14 < E_{\text{Bi}}^0 = 0.32$) and not stoichiometrically ($\text{In} > \text{Bi} > \text{Sn}$) suggesting a redox-driven speciation/differentiation, ii) confirms TOCI, iii) a two-step oxidation process in the formation of the oxide shell, iv) the native oxide in Field's metal liquid particles is thin (<10 nm) but grows with heating, and v) the Bi surface features are extruded upon cooling with concomitant surface oxidation of the metal. Based on the oxidation theories (Fig 1a-c) there is a possibility of creating an oxide shell in the Wagner regime where increase in oxidation does not lead to tight uniform growth on the inside due to localized growth of the oxide crystals. This would result in an oxide shell on the thermally expanded metal surface leading to an oxide shell that is larger than the solidified metal. In this case, there would be enough room for a solidifying NTE

metal to remain in the now speleothem-like shell. Alternatively, enriching a higher E° PTE component can lead to similar entrapment. In both cases, the molten metal would freely flow over stalagmite-like features and with solidification would

create oxide-metal-oxide features. To illustrate this ansatz, we treated BiSn and InSn like the Field's metal and analyzed their core structures.

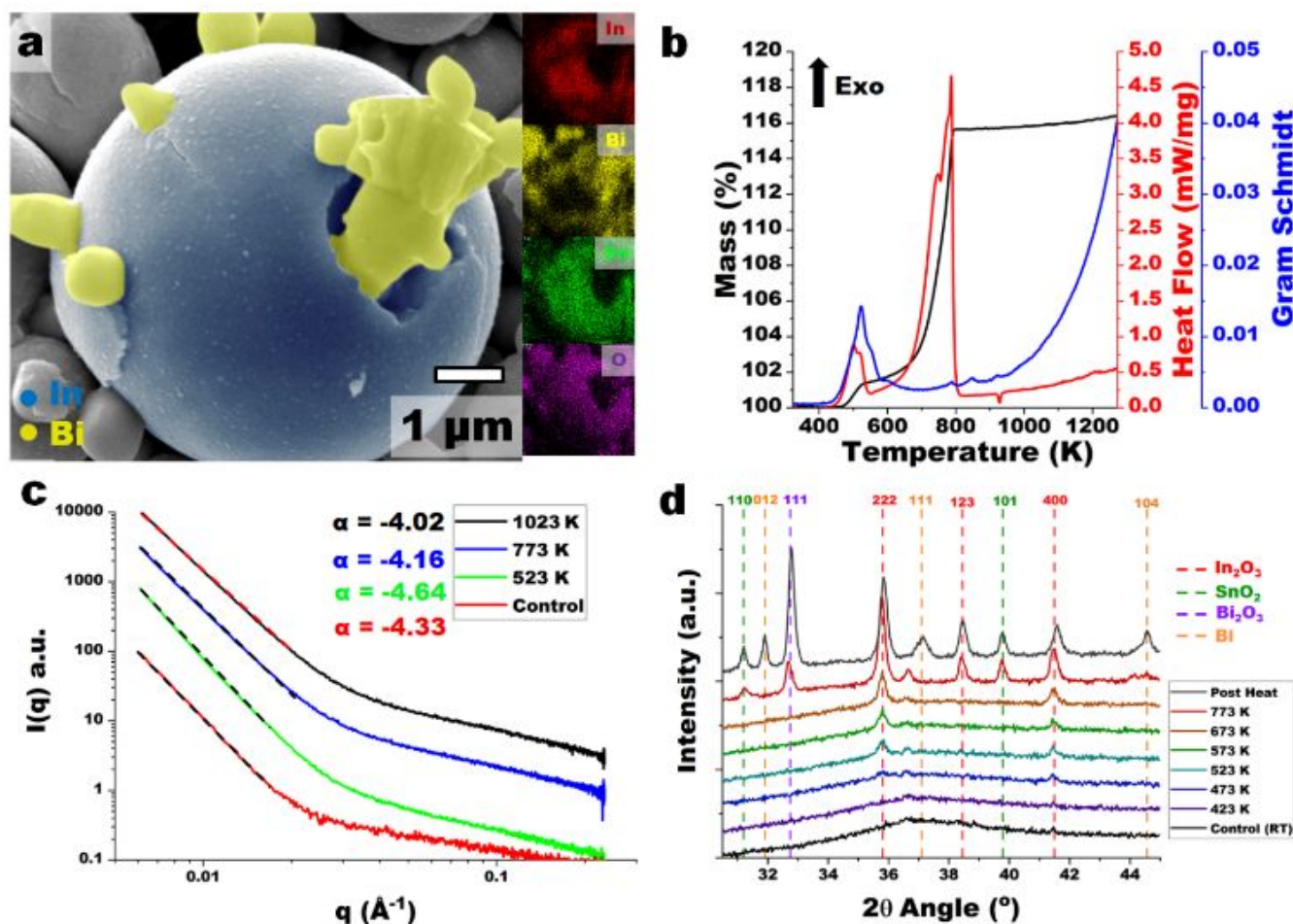


Figure 3. (a) EDS Map of Field's metal particle heat treated at 873 K with 30 minutes isothermal time. (b) DSC-TGA-Gram Schmidt plot of heat-treated particles up to 1273 K. (c) SAXS dimensional analysis for particles heat-treated at different temperatures. (d) HTXRD of Field's metal particles. False coloring: blue indicates native, indium rich oxide and yellow: bismuth rich region.

Furthermore, the chemical process of converting liquid metal to a solid through oxidation is well-understood.^{30, 32, 43} The process is diffusion-based for oxide metal layers of sufficient thickness, i.e. the Wagner regime. In this region the growth rate is proportional to an oxidizer concentration gradient across the oxide metal layer.^{30, 32, 43} Thus, the bulk liquid metal removal rate for the fastest oxidizing metal is proportional to the oxide layer growth rate and the oxidant concentration gradient, which decreases as the oxide layer grows. This may lead one to believe the fastest reacting metal oxide layer growth should be self-limiting as the concentration gradient reduces. Mass transport in the bulk liquid metal phase is, however, also diffusion-limited due to the small length scales (small liquid volumes) discussed in this study. Therefore, the oxide layer growth rate and bulk removal are coupled. A balance between a bulk planar diffusion process and the interface (solid-liquid) concentration based growth rate would suggest $D \frac{\partial^2 c}{\partial x^2} = \frac{\partial c}{\partial t}$ (where D is fastest reacting bulk liquid metal diffusivity of concentration c) but with $\frac{\partial c}{\partial t} \propto \Delta c_{ox}/x$ (where

Δc_{ox} is the ambient oxidizer concentration) the removal of fastest oxidizing metal from the bulk suggests a logarithmic flux i.e. $\frac{\partial c}{\partial x} \propto \ln x$. Thus, the removal of the fastest oxidizing metal may be sustained throughout the growth process even when the identity of this species is changing with depletion of one alloy component. In light of this rate argument, sequential depletion of alloy components justifies the observed enrichment of the highest redox component in the bulk, allowing us to design a redox-based purification process.

Ship in a Bottle

Particles of BiSn (eutectic, Bi:Sn 58:42 wt%, or 44:56 at%, $T_m = 411$ K) and InSn (eutectic, In:Sn 52:48 wt%, or 53:47 at%, $T_m = 391$ K) were prepared using the SLICE method.³⁹ The particles were undercooled to 264 K (BiSn) and 335 K (InSn) ensuring a liquidus phase far below temperatures of interest (Figure S1). For the BiSn samples, we observed that upon heating to 773 K the particles appeared wrinkled with minimal emergent surface

texturing (Figure 4a). Further heating to 873 K (Figure 4b) or higher (Figure S8) increases wrinkling of the shell with analogous two-step transition events as with Field's metal, albeit at different temperatures (Figure S8e). Examining the cross-section of these particles reveals a trapped Bi-rich core albeit with significant void volume (Figure 4c, Figure S9-10 and Supporting Video SV2-3) suggesting that the observed wrinkling was due to thermal contraction. Unlike in ambient liquid metal particles that only develop a hollow core upon complete oxidation,^{18, 19} the growth of crystallites, solidification, and concomitant separation/speciation triggers asymmetry in expansive work enabling formation of voids. Furthermore, BiSn contains high level of Bi (higher E°) and thus depletion of the readily oxidizing component (Sn) is further enhanced, whilst Bi stays in the core. In this case, therefore, stoichiometry surpasses effect of thermal expansivity observed with Field's metal. Elemental analysis reveals the shell and growing crystallites to be predominantly SnO_2 . To further confirm these changes, HTXRD analysis of the particles showed poor crystallinity in the as-synthesized BiSn particles with SnO/SnO_2 peaks becoming prominent at 773 K albeit with concomitant generation of yet to be assigned peaks (Figure S11a). As expected, diffraction peaks increase with continued heating. The enrichment indicates a clear separation/dealloying of the material with higher E° ($E_{\text{Bi}}^\circ = 0.32$, $E_{\text{Sn}}^\circ = -0.14$; $\Delta E^\circ = 0.46$) component isolating into the core. Interestingly, and as hypothesized, we observe entrapment of a growing oxide crystallite by the metal, which we infer are forming upon cooling (Figure 4c). The observed engulfment (Figure 4c) shows a growing crystal that was partially encumbered by the metal, indicating that it is possible to fully encapsulate a growing crystallite inside a metal where the proportion of the metal/enriched core phase is high. This hypothesis is, however, limited by stoichiometry and requires almost equivalent proportions of the two elements in the binary alloy.

Comparatively, BiSn has 12% more of the lower E° component and a large difference in redox potential ($\Delta E^\circ = 0.46$), while InSn presents a narrower redox gap ($E_{\text{In}}^\circ = -0.32$, $E_{\text{Sn}}^\circ = -0.14$, $\Delta E^\circ = 0.18$) and only a slight (6%) enrichment in the lower E° component. In this case, we anticipate that surface oxidation in the Wagner regime would lead to significant growth of the dominant oxidizing species in the form of In_2O_3 crystallites and/or a thick oxide shell with Sn-rich phase trapped in the core. We observe that InSn particles show significant thermal stress spallation when heated to 773 K (Figure 4d) and 873 K (Figure 4e and S12-13). Cross-section of these particles reveal a 'ship-in-a-bottle' in that the oxide is completely engulfed in the Sn-metal—an advanced stage of engulfment compared to that observed in BiSn (Supporting Video SV4). Elemental analysis by EDS (Figure 4f) confirms the distribution of the components. Given that these particles undercool down to 335 K, XRD diffraction patterns of the control reveal presence of In, Sn and In_2O_3 with SnO/SnO_2 diffraction peaks only appearing after heat-treatment (Figure S11b).

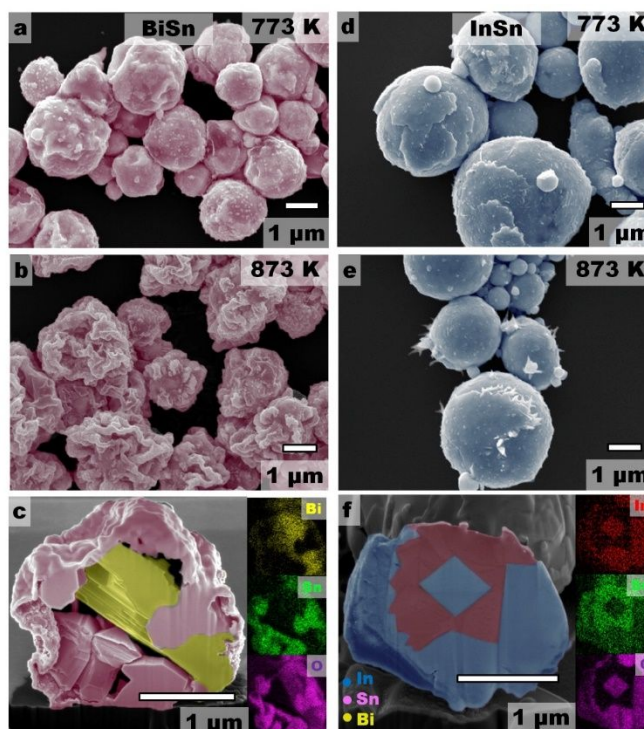


Figure 4. SEM images of BiSn and InSn particles heat treated at (a,d) 773 K, (b,e) 873 K along with (c) EDS map of FIB sectioned BiSn particle heat treated at 873 K and (f) InSn particle heat treated at 873 K. False coloring: blue indicates indium rich region, yellow: bismuth rich region and pink: tin rich region.

Conclusions

This work demonstrates the controlled behaviour of surface oxidation in metals and its potential in design of new particle structures or purification/dealloying. By tuning oxidation via temperature, oxidant partial pressure, time and composition, a balance between reactivity and thermal deformation enables unprecedented morphologies. By trapping these features through solidification, we can stabilize them below the materials melting point. Specifically, we infer the following:

- i. Metals undergo extended multi-step oxidation processes with temperature. These stages are; i) the stochastic stoichiometric oxidation stage to create the first pre-Cabrera-Mott film, ii) the Cabrera-Mott regime, iii) the intermediate XRB regime, and iv) Wagner regime. All these stages depend on amount of existing oxide film except for the statistical mechanics driven initial state when the bare metal surface is exposed to the oxidant.
- ii. Despite changing mechanisms, we exploit these processes to selectively induce dealloying leading to speciation into the growing oxide and concomitant purification/isolation of the highest E° component to the core of the particle. Coupling the solidification to oxide growth leads to new particle morphologies analogous to macroscopic cave-formation (speleothem) albeit filled with the metal.
- iii. We paired oxidation rate laws to thermal expansivity to deploy alloy composition, stoichiometry and properties of the growing oxides to create dissimilar particle

morphologies. For alloys where the NTE component has a significantly large ΔE° difference to the most reactive components and is a minor component of the alloy (e.g. Field's metal), depletion of other elements allows for the extrusion of this component upon solidification. On the contrary, where the concentration of the NTE component is high, inward growth of the oxide may be insufficient to occupy all the space occupied by the expanded metal (e.g. in BiSn). In this case the metal solidifies onto the growing crystallites leading to 'ship-in-a-bottle' oxide-metal-oxide morphologies.

- iv. We also illustrate that although thermal expansivity is crucial, stoichiometric considerations may surpass asymmetry in volumetric changes as illustrated by Field's metal vs BiSn. A balance of total thermal expansive work is therefore essential in realizing the desired structures and/or morphologies.

Conflicts of interest

There are no conflicts to declare.

Acknowledgements

This work was supported by Iowa State University through start-up funds to MT and in part through a DOE SBIR grant number DE-SC0018791. The authors would like to thank Matt Besser (Ames Lab) for the assistance in HTXRD Experiment. Ames Laboratory is operated for the U.S. Department of Energy by Iowa State University. We thank Dr. Ian Tevis for the Field's metal FIB experiments. The SAXS instrumentation was acquired through NSF grant NSF-DMR-1626315.

References

1. A. Martin, C. Du, B. Chang and M. Thuo, *Chem. Mater.*, 2020, DOI: 10.1021/acs.chemmater.0c02047.
2. R. N. S. Sodhi, P. Brodersen, L. Cademartiri, M. Thuo and C. A. Nijhuis, *Surf. Interface Anal.*, 2017, **49**, 1309-1315.
3. A. Zangwill, *Physics at Surfaces*, Cambridge University Press, Cambridge, 1988.
4. H.-J. Butt, K. Graf and M. Kappl, *Physics and Chemistry of Interfaces, Third Edition*, Wiley-VCH, 2013.
5. A. Martin, B. S. Chang, A. M. Pauls, C. Du and M. M. Thuo, *Angew. Chem. Int. Ed.*, 2020, DOI: <https://doi.org/10.1002/anie.202013489>.
6. J. Chen, T. J. Giroux, Y. Nguyen, A. A. Kadoma, B. S. Chang, B. VanVeller and M. M. Thuo, *Phys. Chem. Chem. Phys.*, 2018, **20**, 4864-4878.
7. M. D. Dickey, *ACS Appl. Mater. Interfaces*, 2014, **6**, 18369-18379.
8. M. D. Dickey, *Adv. Mater.*, 2017, **29**, 1606425.
9. M. D. Dickey, R. C. Chiechi, R. J. Larsen, E. A. Weiss, D. A. Weitz and G. M. Whitesides, *Adv. Funct. Mater.*, 2008, **18**, 1097-1104.
10. B. S. Chang, R. Tutika, J. Cutinho, S. Oyola-Reynoso, J. Chen, M. D. Bartlett and M. M. Thuo, *Mater. Horiz.*, 2018, **5**, 416-422.
11. J. J. Chang, A. Martin, C. Du, A. Pauls and M. M. Thuo, *Angew. Chem. Int. Ed.*, 2020, **59**, 16346-16351.
12. A. Martin, B. S. Chang, Z. Martin, D. Paramanik, C. Frankiewicz, S. Kundu, I. D. Tevis and M. Thuo, *Adv. Funct. Mater.*, 2019, **29**, 1903687.
13. B. S. Chang, M. Fratzl, A. Boyer, A. Martin, H. C. Ahrenholtz, I. De Moraes, J.-F. Bloch, N. M. Dempsey and M. M. Thuo, *Ind. Eng. Chem. Res.*, 2019, **58**, 4137-4142.
14. B. S. Chang, B. Thomas, J. Chen, I. D. Tevis, P. Karanja, S. Çınar, A. Venkatesh, A. J. Rossini and M. M. Thuo, *Nanoscale*, 2019, **11**, 14060-14069.
15. A. Martin, C. Du, A. M. Pauls, T. Ward and M. Thuo, *Adv. Mater. Interfaces*, 2020, **7**, 2001294.
16. L. Cademartiri, M. M. Thuo, C. A. Nijhuis, W. F. Reus, S. Tricard, J. R. Barber, R. N. S. Sodhi, P. Brodersen, C. Kim, R. C. Chiechi and G. M. Whitesides, *J. Phys. Chem. C*, 2012, **116**, 10848.
17. Z. J. Farrell and C. Tabor, *Langmuir*, 2018, **34**, 234-240.
18. J. Cutinho, B. S. Chang, S. Oyola-Reynoso, J. Chen, S. S. Akhter, I. D. Tevis, N. J. Bello, A. Martin, M. C. Foster and M. M. Thuo, *ACS Nano*, 2018, **12**, 4744-4753.
19. A. Martin, W. Kiarie, B. Chang and M. Thuo, *Angew. Chem. Int. Ed.*, 2020, **59**, 352-357.
20. M. Bernhard, F. E. Brinckman and K. J. Irgolic, Berlin, Heidelberg, 1986.
21. S. Çınar, I. D. Tevis, J. Chen and M. Thuo, *Sci. Rep.*, 2016, **6**, 21864.
22. Z. Xu, K. M. Rosso and S. Bruemmer, *Phys. Chem. Chem. Phys.*, 2012, **14**, 14534-14539.
23. H. Over and A. P. Seitsonen, *Science*, 2002, **297**, 2003-2005.
24. S. R. J. Saunders, M. Monteiro and F. Rizzo, *Prog. Mater. Sci.*, 2008, **53**, 775-837.
25. J. T. Law, *J. Phys. Chem.*, 1957, **61**, 1200-1205.
26. N. Cabrera and N. F. Mott, *Rep. Prog. Phys.*, 1949, **12**, 163-184.
27. W. Carl, *Z. Phys. Chem.*, 1933, **21B**, 25-41.
28. R. Carter, F. Richardson and C. Wagner, *JOM*, 1955, **7**, 336-343.
29. L. Himmel, R. Mehl and C. E. Birchenall, *JOM*, 1953, **5**, 827-843.
30. A. Atkinson, *Mater. Sci. Technol.*, 1988, **4**, 1046-1051.
31. A. Atkinson, *Rev. Mod. Phys.*, 1985, **57**, 437-470.
32. A. Atkinson, *Oxidation of metals and associated mass transport*, The Metallurgical Society of AIME, Warrendale, PA, 1987.
33. L.-L. Wang and D. D. Johnson, *J. Am. Chem. Soc.*, 2009, **131**, 14023-14029.
34. R. Shuttleworth, *Proc. Phys. Soc., London, Sect. A*, 1950, **63**, 444.
35. M. F. Dumke, T. A. Tombrello, R. A. Weller, R. M. Housley and E. H. Cirlin, *Surf. Sci.*, 1983, **124**, 407-422.
36. J. Lowengrub, J. Xu and A. Voigt, *Fluid Dyn. Mater. Proc.*, 2007, **3**, 1-19.
37. P. Fischer, I. Sosnowska and M. Szymanski, *J. Phys. C*, 1978, **11**, 1043.
38. E. Cave and L. Holroyd, *J. Appl. Phys.*, 1960, **31**, 1357-1358.
39. I. D. Tevis, L. B. Newcomb and M. Thuo, *Langmuir*, 2014, **30**, 14308-14313.
40. W. Ruland, *J. Appl. Cryst.*, 1971, **4**, 70-73.
41. M. Björkqvist, J. Salonen and E. Laine, *J. Appl. Cryst.*, 2003, **36**, 740-743.
42. G. Porod, *Kolloid-Z*, 1951, **124**, 83-114.

COMMUNICATION

Journal Name

43. C. Wagner, *Z. Phys. Chem.*, 1933, **21**, 25-41.